

MIT Open Access Articles

Assessment of a field-aligned ICRF antenna

The MIT Faculty has made this article openly available. **Please share** how this access benefits you. Your story matters.

Citation: Wukitch, S. J., D. Brunner, P. Ennever, M. L. Garrett, A. Hubbard, B. Labombard, C. Lau, et al. "Assessment of a Field-Aligned ICRF Antenna" AIP Conference Proceedings, 1580, 73 (2014) p.73-80.

As Published: <http://dx.doi.org/10.1063/1.4864504>

Publisher: American Institute of Physics (AIP)

Persistent URL: <http://hdl.handle.net/1721.1/88535>

Version: Original manuscript: author's manuscript prior to formal peer review

Terms of use: Creative Commons Attribution-Noncommercial-Share Alike



Assessment of a Field-Aligned ICRF Antenna*

S.J. Wukitch, D. Brunner, P. Ennever, M.L. Garrett, A. Hubbard, B. Labombard, C. Lau, Y. Lin, B. Lipschultz, D. Miller, R. Ochoukov, M. Porkolab, M.L. Reinke, and J.L. Terry

MIT Plasma Science and Fusion Center, 190 Albany St Cambridge, 02139, USA.

Abstract. Impurity contamination and localized heat loads associated with ion cyclotron range of frequency (ICRF) antenna operation are among the most challenging issues for ICRF utilization.. Another challenge is maintaining maximum coupled power through plasma variations including edge localized modes (ELMs) and confinement transitions. Here, we report on an experimental assessment of a field aligned (FA) antenna with respect to impurity contamination, impurity sources, RF enhanced heat flux and load tolerance. In addition, we compare the modification of the scrape of layer (SOL) plasma potential of the FA antenna to a conventional, toroidally aligned (TA) antenna, in order to explore the underlying physics governing impurity contamination linked to ICRF heating. The FA antenna is a 4-strap ICRF antenna where the current straps and antenna enclosure sides are perpendicular to and the Faraday screen rods are parallel to the total magnetic field. In principle, alignment with respect to the total magnetic field minimizes integrated E_{\parallel} (electric field along a magnetic field line) via symmetry. Consistent with expectations, we observed that the impurity contamination and impurity source at the FA antenna are reduced compared to the TA antenna. In both L and H-mode discharges, the radiated power is 20-30% lower for a FA-antenna heated discharge than a discharge heated with the TA-antennas. Further we observe that the fraction of RF energy deposited upon the antenna is less than 0.4 % of the total injected RF energy in dipole phasing. The total deposited energy increases significantly when the FA antenna is operated in monopole phasing. The FA antenna also exhibits an unexpected load tolerance for ELMs and confinement transitions compared to the TA antennas. However, inconsistent with expectations, we observe RF induced plasma potentials to be nearly identical for FA and TA antennas when operated in dipole phasing. In monopole phasing, the FA antenna has the highest plasma potentials and poor heating efficiency despite calculations indicating low integrated E_{\parallel} . In mode conversion heating scenario, no core waves were detected in the plasma core indicating poor wave penetration. For monopole phasing, simulations suggest the antenna spectrum is peaked at very short wavelength and full wave simulations show the short wavelength has poor wave penetration to the plasma core.

Keywords: ICRF, antenna, plasma material interaction

PACS: 52.40.Fd, 52.50.Qt, 52.25.Vy, 52.40.Hf, 52.55.Fa, 52.70.Ds

INTRODUCTION

Ion cyclotron range of frequency power is considered a good candidate for experiments, like ITER and future reactors, to provide bulk heating[1]. This derives, in part, from the fact that ICRF has been experimentally demonstrated to heat high performance plasmas in a number of experiments including deuterium-tritium discharges on TFTR[2] and JET[3], and has favorable scaling to burning plasmas. Unlike the previous generation of fusion experiments, the plasma facing components (PFCs) for future reactors and a growing number of experiments are high Z metals, [AUG, JET, C-Mod], due to concerns regarding material erosion and tritium retention with carbon.[4] Since the plasma tolerance for high Z impurities is significantly less than light impurities, impurity contamination associated ICRF antenna operation becomes more challenging. In addition to impurity contamination, RF enhanced heat flux of the antenna and antenna load tolerance can limit ICRF utilization.

Impurity contamination with ICRF may be a result of increased impurity source due to RF enhanced sheaths resulting in higher sputtering:[5] transport modification due to convective cells:[6] or a combination. The precise physics responsible for impurity contamination with ICRF is yet unclear and detailed phenomenology often differs from experiment to experiment. For example, C-Mod data suggest important RF impurity sources are located away from the antenna and that low Z impurity seeding reduces the core molybdenum concentration.[7] ASDEX-U ICRF experiments indicated that the local RF limiters are the primary impurity source.[8] Early work on RF impurity contamination at JET suggested that the Faraday screen was a primary source.[9] More recent work has identified additional sources away from the antenna as important contributors.[10]

To utilize ICRF in steady state, RF enhanced heat flux needs to be managed to prevent exceeding the power handling capability of the antenna and other PFCs. RF enhanced heat flux is thought to be a result of RF enhanced

sheaths which increases the energy per ion and transport modification due to convective cells that can increase the particle flux. In ITER, the ICRF antenna design assumes an RF enhanced heat flux of 6 MW/m^2 which corresponds to $\sim 125 \text{ kW}$ out of 20 MW injected power or 0.625% . [11] The experimental results from JET indicate between 2-10% of the injected power is found on the antenna limiters and septum. [12] Tore Supra has also made extensive measurements and have shown that 3.5% of the injected power is found locally on the antenna. [13]

To maintain coupled power to the plasma, an ICRF antenna needs to be load tolerant either intrinsically or through external matching. Antenna coupling is determined primarily by the density profile in the plasma edge. In C-Mod, the profile of interest is the scrape off layer to the top of the density pedestal. Thus plasma load variations are encountered during confinement transitions and edge localized mode (ELMs) activity. In C-Mod, the resistive load of the antenna is dominated by the antenna reactance. Thus, load variations due to changes in the resistive load should primarily result in changes in magnitude of the reflection coefficient rather than its phase. For the C-Mod toroidally aligned (TA) antenna, the load variation appears to a combination of antenna resistance and reactance.

We have recently installed a field aligned (FA) antenna, shown in Figure 1, primarily to investigate whether a FA antenna has lower impurity contamination associated with RF antenna operation than a toroidally aligned antenna. In C-Mod, we have observed that the core molybdenum contamination and antenna molybdenum impurity sources is correlated with ICRF power from the TA antennas. [14] On open field lines, the plasma potentials, scrape off layer (SOL) density profiles, and SOL transport is modified during operation of our conventional TA antennas. The RF impact on the plasma edge is thought to result from unwanted parallel electric fields (E_{\parallel}) and the FA antenna design aims to reduce the integrated E_{\parallel} through field line symmetry. This approach is derived in part from previous experimental work that showed reduced impurity contamination with dipole phasing compared with monopole phasing. The reduction in impurity contamination has been interpreted to be due to a reduction in the integrated E_{\parallel} for dipole phasing. [15] This interpretation is independently confirmed by antenna – plasma simulations using a finite element method electromagnetic solver with a cold plasma dielectric that show a reduction in E_{\parallel} for dipole phasing relative to monopole phasing, see Figure 2.

The FA antenna is a 4-strap, ICRF antenna using a folded strap design due to limited space. The current straps and antenna box structure are perpendicular and the Faraday screen (FS) is parallel to the total magnetic field. For comparison, the C-Mod conventional TA ICRF antennas have end fed center grounded current straps. The current straps and antenna structure are perpendicular and the FS rods are parallel to the total magnetic field. Since the total magnetic field pitch has a range between $7\text{-}13^\circ$ in C-Mod, the FA-antenna is aligned to a 10° field pitch. The FA antenna has a similar strap spacing as our TA antenna and the vacuum spectrum peaks at toroidal wave number ~ 13 . The FA antenna has a radiating surface area of 0.33 m^2 ; thus, the expected ITER ICRF antenna power density of 6 MW/m^2 is achieved at 2 MW coupled power. The antenna protection tiles and FS rods are TiCN coated TZM molybdenum. The tiles are located 3 mm behind the main plasma

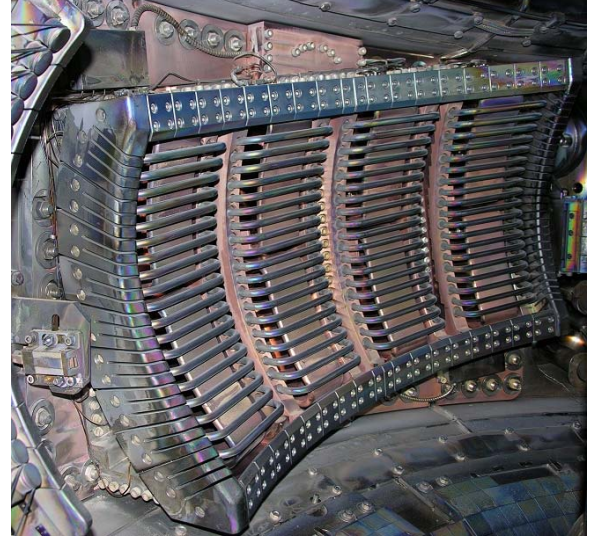


Figure 1: Field aligned antenna after its first experimental campaign in Alcator C-Mod. The antenna is perpendicular to a field line at 10° from horizontal. Scrape of layer X-mode reflectometer horns are located left of the field aligned antenna.

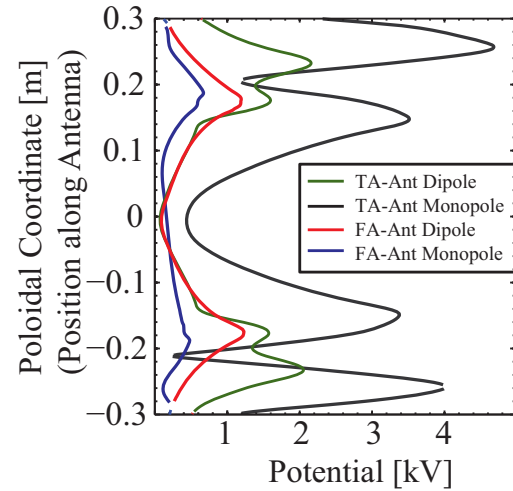


Figure 2: Calculated integrated E_{\parallel} fields for the FA and TA antennas where the poloidal coordinate is the position along the antenna box centered on the antenna. For our conventional TA antennas, this is the poloidal coordinate. For conventional TA antennas, the integrated E_{\parallel} is lower for dipole phase. In the FA antenna, the integrated E_{\parallel} is lower than the conventional and monopole phase has the lowest integrated E_{\parallel} .

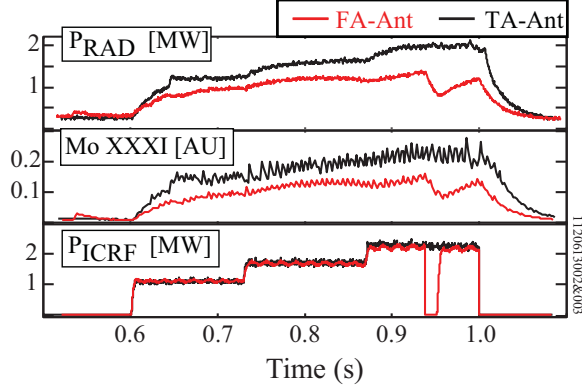


Figure 3: Comparison of the plasma radiation and core molybdenum impurity response to the FA and TA antennas. The radiated power and core molybdenum traces show that the FA antenna has significantly lower radiated power and core molybdenum.

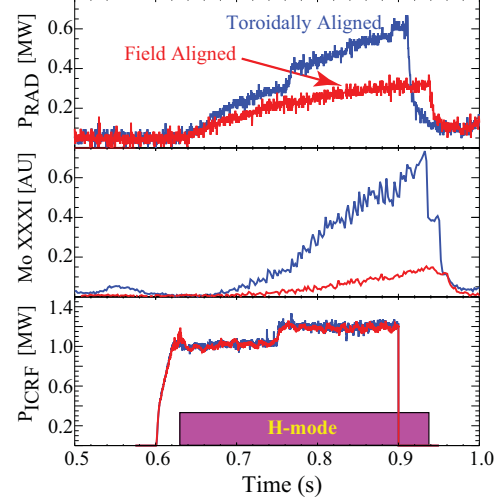


Figure 4: In H-mode, the radiated power and core molybdenum are reduced for the FA antenna relative to TA antenna.

limiter and the FS is 5 mm behind the antenna protection tiles. The FA-antenna has been analyzed using a full 3-D antenna model with a cold plasma using finite element method.[16] Compared to the TA antenna, the FA-antenna has reduced integrated $E_{||}$ and a $\sim 50\%$ reduction in the local $E_{||}$ fields. The reduction in the integrated $E_{||}$ is phase dependent with the smallest reduction for dipole phasing, factor of 2-3. For monopole phasing, the integrated $E_{||}$ is lower than dipole which is in contrast to the results from the TA antenna, see Figure 2.

In the experiments presented here, H minority heating scenario is used to heat deuterium discharges where the H minority concentration is typically 2-10%. The FA and TA antennas are operated at 78 MHz and 80 MHz, respectively, and the RF power is 0.2-2.5 MW. The magnetic field is typically 5.2-5.4 T and plasma current from 0.6-1.3 MA. The typical average densities are $0.75\text{-}1.2 \times 10^{20} \text{ m}^{-3}$ for L-mode discharges and H-modes have similar target densities. In addition to standard plasma diagnostics, the local impurity sources are monitored using an f/4, 0.25 m visible spectrometer with discrete views of both the main plasma limiter, FA antenna, and TA antennas. The typical lines monitored are Mo I and Ti I. The core impurity content is monitored using two flat-field spectrometers: 10-30 nm (Mo XXXI (11.6 nm), Mo XXXII (12.8 nm)) for mid-Z elements and 1-10 nm for low Z materials and total plasma radiation is monitored with bolometers. We have two SOL X-mode reflectometers: one is located next to FA antenna as seen in Figure 1 and another set of horns near the TA antennas. We utilize gas puff imaging and emissive probes to monitor plasma potential. The GPI and emissive probes map to the FA antenna only over a limited range plasma of plasma current. In addition, 10 out of 18 antenna protection TZM tiles are instrumented with fast response thermocouples and provide net energy deposited.

ANTENNA CHARACTERIZATION

Impurity Contamination and Antenna Impurity Sources

To characterize the impurity contamination associated with the FA antenna, a series of discharges were performed where the ion grad-B drift is directed away from the active X-point resulting in a high H-mode power threshold. Using up to 2.5 MW coupled power, the plasma response to RF power from the FA and TA are compared in consecutive discharges prior to the first boronization where the H fraction was between 8-10%. A typical discharge comparison is shown in Figure 3. The radiated power and core molybdenum contamination is lower for the FA antenna. The reduction in radiated power is 0.4-0.6 MW per 2.5 MW injected RF power.

Post boronization, similar experiments were performed in H-mode discharges and an example discharge comparison is shown in Figure 4. The core molybdenum contamination is significantly lower for the H-mode heated by the FA antenna than that heated by the TA antennas. The difference in core molybdenum contamination is also reflected in the difference in the delay in H to L back transition. In addition the core radiated power increases more slowly for the FA-antenna compared to the TA antenna heated H-mode. The overall plasma response, however, is similar for the two antennas suggesting similar heating effectiveness in H-mode and H-mode threshold. In these H-modes, molybdenum does not appear to be the dominant contributor to the radiated power.

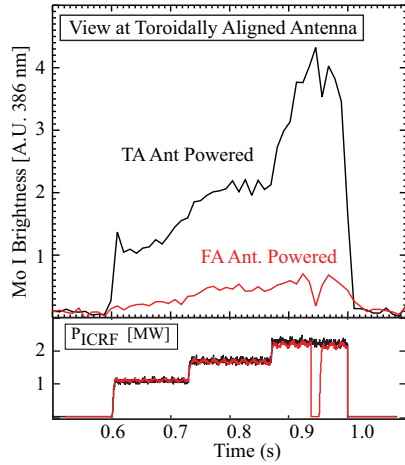


Figure 5: For the view of the TA antenna, the Molybdenum I signal responds strongly to RF coupled from the TA antenna (black trace) and approximately doubles for each 0.75 MW power step. The molybdenum I signal response when the FA antenna is powered is significantly less.

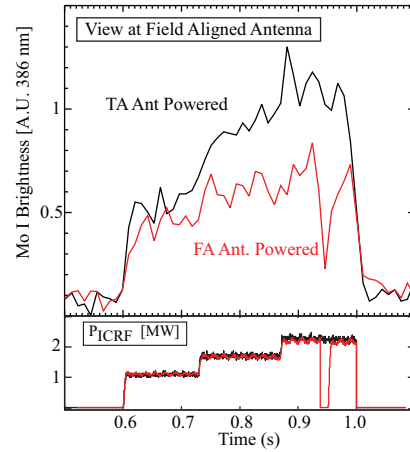


Figure 6: For the view of the FA antenna, the Molybdenum I signal responds strongly to RF coupled from the TA antenna (black trace) and approximately doubles for each 0.75 MW power step. The molybdenum I signal response when the FA antenna is powered is significantly less.

To characterize a local antenna impurity sources, the molybdenum I and titanium I lines are monitored: 4 views cover the FA antenna and two to cover the TA antennas. Prior to boronization, L-mode discharges are utilized to compare the impurity source response at the TA and FA antennas when either the TA or FA antenna is powered. In Figure 5, we concentrate on molybdenum source at the TA antenna. The RF power is increased in three steps: 1 MW (0.6-0.725 s) to 1.75 MW (0.725-0.875 s) to 2.5 MW (0.875-1 s). The first panel is the molybdenum I signal (386.4 nm) from a view at the TA antenna and the second panel is of the RF power trace. In the TA antenna view, the molybdenum I signal responds strongly when the TA antenna is powered (shown in black) and is proportional to the injected power as expected. The molybdenum I signal approximately doubles for each 0.75 MW step. When the FA antenna is powered, the molybdenum I signal responds weakly (shown in red) for the TA antenna view. In Figure 6, the molybdenum I signal response for FA antenna view is shown. When the TA antenna is powered (black trace), the molybdenum I signal responds more strongly when the TA antenna is powered (red trace). The results are qualitative since the views are not cross calibrated. These measurements suggest the impurity source at the FA antenna is lower when the FA antenna is powered than when the TA antenna is powered. Furthermore, views monitoring the main plasma limiter show that the FA antenna has lower molybdenum I signal response compared to the TA antennas.

Heat Flux to Antenna

To monitor heat flux to the FA antenna, the antenna is instrumented with 10 thermocouples in the antenna side protection tiles and there are 9 side tiles one each side of the antenna. The thermocouples are located in #1, #4, #5, #6, and #9 where tiles #1 and #9 correspond to the top and bottom tiles, respectively. The side protection tiles are expected to receive the majority of the heat flux to the antenna because they shadow the FS rods, top and bottom tiles by 5 mm and 3 mm, respectively. In C-Mod, the density decay length is ~ 3 mm so the FS, top and bottom tiles are between 1-1.6 density decay lengths. Post campaign inspection shows thermal damage only to the four corner tiles and this is consistent with thermocouple measurements. In practice, 5 thermocouples on the left side of the FA antenna were operational for the entire campaign and are the source of the measurements presented below. To accurately measure the temperature response of molybdenum tile, thermojunction is pressed in direct contact with the molybdenum tile. The temperature of the tile is measured before and after the pulse. With the tile mass, the energy deposited on the tile during the discharge can be calculated.

We analyze the thermocouple data over a three month operational period that includes a variety of discharges: L-mode, H-mode, $I_p = 0.6-1.3$ MA, outer gap = 0.5-2 cm, and antenna phase. As done for the antenna impurity source comparison, we isolated the discharges heated with FA antenna (63 discharges) from discharges heated with TA antenna (111 discharges). In Figure 7, the total number of Joules measured on the antenna left side protection tiles is plotted against number of Joules coupled to the plasma by the antenna. The contribution from the ohmic heating is ignored. The discharges heated with the FA antenna have lower total energy deposited on the side protection tiles than for discharges heated with the TA antenna except for four circled data points that utilized for monopole phasing.

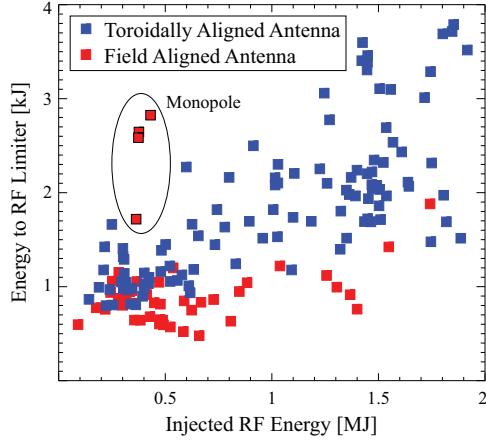


Figure 7: The total energy deposited on tiles #1, #4, #5, #6, and #9 side protection tiles of the FA antenna when field aligned is powered (red squares) is lower than when the toroidally aligned antenna (blue squares) is powered.

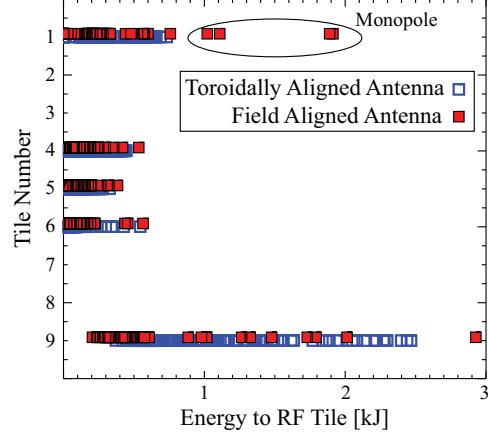


Figure 8: Deposited energy profile on the FA side protection tiles shows that the profile is little different whether the FA or the TA antenna is powered. For monopole phase, tile #1 receives significantly more energy.

In Figure 8, the energy deposited per tile is plotted to provide an indication of spatial distribution. The primary conclusion is that the profile is similar regardless of which antenna is powered. For tile 9, the heat load increases with increasing power from the TA antenna, power from lower hybrid or locked mode discharges which accounts for the set of data points at above 0.8 kJ when the FA antenna is powered. The heat flux increases significantly for monopole phasing when the FA antenna is powered and is concentrated on tile 1. The heat flux to the antenna follows the trend observed for the impurity sources at the FA antenna: the FA antenna appears to have heat flux levels similar to that from the TA antenna when the FA antenna is operated in dipole phasing. We estimate the total power deposited upon the limiter tiles as a fraction of the total coupled RF energy by extrapolating from the measurements. We linearly interpolate the energy deposited on tiles #2, #3, #7, and #8 which roughly doubles the measured deposited energy. Assuming an equal amount on the right set of side protection tiles, the total deposited energy is ~ 6 kJ for 1.5 MJ injected or 0.4%. For comparison, the ITER design is 0.625% of 20 MW.

Antenna Coupling

The FA antenna has electrical performance has been reasonable: achieved power densities up to 9 MW/m^2 and a maximum voltage of 45 kV. Due to lower loading in H-mode, the maximum power can be limited to 2 MW because the maximum voltage is reached prior to reaching the transmitter power limit. The higher loading in L and I-mode allows the maximum coupled power to reach 3 MW. The FA-antenna neutral pressure limit (pressure at which the antenna voltage handling degrades dramatically) also exceeds the limit for the TA antennas. The voltage limitation is related to the limited space available in C-Mod rather than a feature of a FA antenna design. An antenna based on an end fed center grounded strap would have significantly lower strap inductance and increase the maximum power for the applied voltage. For C-Mod this would require additional ports to be added to the vacuum vessel.

For the FA aligned antenna, the antenna loading and dependence on plasma current was a concern since the antenna design was selected for an average plasma helicity. We have found that the FA antenna loading is similar to TA antennas over a broad range of plasma currents and densities. This suggests the field alignment does not significantly impact the resistive part of the antenna impedance and that the density profile determines the resistive loading. The reduced variation in the reflection coefficient also results in the FA antenna having greater load tolerance. A comparison of the reflection coefficient from both the FA (red) and TA (blue) antenna for an ELMing discharge is shown in Figure 9. The space occupied by the FA antenna on the Smith chart is significantly less and in practice allowed the antenna to matching network to remain unchanged throughout an experiment despite changes in plasma conditions. In Figure 10, the reflection coefficient during an ELM cycle is shown for both the FA (red) and TA (blue) antenna. Typically, ELMs cause the TA to fault due to the large change in reflected power but for the FA antenna the variation is largely resistive. The reflected power does not exceed the fault level. The physics understanding of the load tolerance is yet to be established. However, we speculate that aligning the antenna has improved the off diagonal terms in the antenna impedance matrix. To illustrate, a generic antenna impedance matrix is shown in Equation 1 for a two strap antenna where: a_{11} and a_{22} are the resistive load provided by the plasma and ohmic losses in the antenna, L_{11} and L_{22} are the strap self inductance, M_{12} and M_{21} are the mutual coupling between the straps, and b_{12} and b_{21}

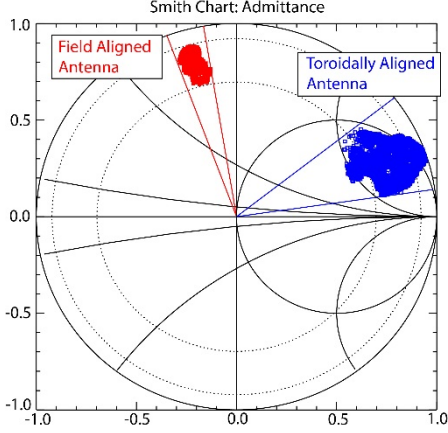


Figure 9: For an ELMing discharge, the field aligned and toroidally aligned antenna reflection coefficient is plotted on a Smith chart and shows that the FA antenna has greater load tolerance.

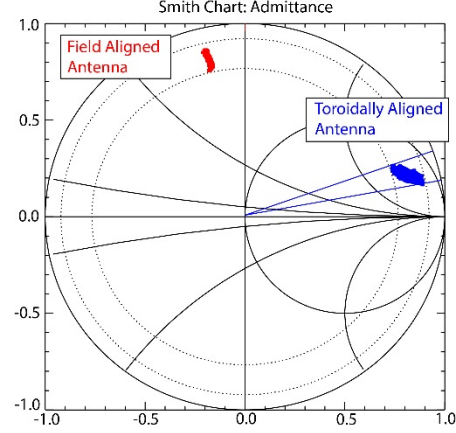


Figure 10: The reflection coefficient during an ELM cycle is plotted on a Smith chart and shows that the FA antenna reflection coefficient (red) variation is largely resistive whereas the TA antenna coefficient (blue) is a combination.

represent the coupling through the plasma. A decoupler can mitigate the fixed imaginary term of the off diagonal terms but the real component, usually about 10-20% of the vacuum mutual

$$Z_{ant} = \begin{bmatrix} a_{11} + jL_{11} & b_{12} + jM_{12} \\ b_{21} + jM_{21} & a_{22} + jL_{22} \end{bmatrix} \quad (1)$$

coupling, can result in large changes in the standing wave pattern.[17] We speculate that $E_{||}$ is reduced such the coupling through the plasma via slow waves is significantly reduced. Future experiments to directly measure the antenna impedance matrix could help clarify the physics governing the improved load tolerance.

Plasma Potential

Reduced $E_{||}$ was hypothesized to lower RF enhanced sheaths. Phenomena (impurity contamination, enhanced impurity sources and heat flux) thought to be driven by $E_{||}$ and the associated enhanced plasma potential are all lower for the FA antenna than the TA antenna suggesting reduced plasma potentials. However, we have measured the plasma potentials associated with the FA and TA antennas using both GPI and emissive probes.[18] For dipole phasing, the maximum plasma potential (found on field lines nearest the radius of the side protection tiles) for the FA antenna is indistinguishable from that measured when the TA antenna is powered as shown in Figure 11. In hindsight, we may have expected this because previous plasma potential measurements of a toroidally aligned antenna at J port –TA@J (antenna replaced by the field aligned antenna) had lower plasma potential than the TA antenna also shown in Figure 11. The impurity contamination however was not remarkably different between the two toroidally aligned antennas. The explanation was that the design details were significantly different which may have influenced the plasma potential measurements.

Dipole versus Monopole

Originally, we thought that a comparison of the FA antenna with dipole and monopole phasing would further test the hypothesis that field alignment would reduce $E_{||}$ and the RF enhanced plasma potential would also decrease. The measured plasma potentials when the FA antenna is operated in monopole phasing is much higher than when the FA antenna is operated in dipole.[18] However, experiments indicate that the elevated plasma potentials and poor heating efficiency is due to poor wave penetration to the plasma core. We performed a series of discharges where the heating scenario is mode conversion heating and the minority ^3He concentration is $\sim 15\%$. The majority of the launched power is absorbed on electrons. As we have in the past, we can monitor the core mode converted wave amplitude and wavenumber spectrum using phase contrast imaging (PCI).[19,20] In mode conversion, monopole is expected to have better mode conversion efficiency due to the lower $k_{||}$ than dipole phasing. As shown in Figure 12, the heating effectiveness is significantly better for dipole than monopole phasing – stored energy and electron temperature increase is proportional RF power. The radiated power and core molybdenum contamination are similar suggesting that difference between monopole and dipole is not dominated by impurity contamination. The carbon II signal responds promptly with application of monopole power indicating the RF is interacting strongly with the SOL. The antenna thermocouples also report a dramatic increase in the energy deposited on the side protection tiles and the X-mode reflectometer shows a remarkable increase in the scrape off layer (SOL) density in front and behind the antenna.

The PCI signal time history is shown in Figure 13. The waves are clearly detected during the period when the FA antenna is operated with dipole phasing and no waves are present when the FA antenna is operated with monopole phasing. This is contrary to the expectation that monopole should have good mode conversion heating. The primary assumption is that the launched $k_{||}$ spectrum utilizes a simplistic antenna geometry: includes only the current straps and does not include the full antenna structure. Utilizing an FEM antenna-plasma model, the antenna spectrum appears to be very short wavelength, approximately half the dipole wavelength. This indicates that the antenna structure including the septa significantly modify the launched spectrum. Similar observations were noted in RANT3D calculations that showed the antenna spectrum was significantly modified by the antenna structure.[21] The simplistic antenna spectrum calculation appears to work for dipole largely because image currents in the septa cancel and have little net effect on the antenna spectrum. From the simple cold wave dispersion relation and TORIC simulations[22], one can readily observe that a wave corresponding to a toroidal mode number of 26 as suggested by the FEM antenna simulation the wave fails to penetrate to the plasma core as shown in Figure 14. Thus, we conclude that the monopole phased antenna has poor heating effectiveness because the wave fails to penetrate to the core.

CONCLUSIONS

The field aligned antenna has improved impurity contamination, lower impurity sources at the antenna, low RF induced heat flux to the antenna, and load tolerance. In both L and H-mode discharges, the radiated power is 20-30% lower for a FA-antenna heated discharge than a discharge heated with the TA-antennas. Further we observe that the fraction of RF energy deposited upon the antenna is $\sim 0.4\%$ of the total injected RF energy in dipole phasing. The FA antenna also exhibits an unexpected load tolerance both for ELMs and confinement transitions compared to the TA antennas. However, inconsistent with expectations, we observe RF induced plasma potentials to be nearly identical for FA and TA antennas when operated in dipole phasing. Antenna operation in monopole phasing has poor heating effectiveness and no waves are detected in the plasma core. The poor heating effectiveness is a result of poor wave penetration to the plasma core.

ACKNOWLEDGMENTS

We greatly appreciate the effort and support of the entire Alcator C-Mod physics, engineering, and operational staff in performing the experiments described here. Work supported by US DOE award DE-FC02-99ER54512 and U.S. DOE Fusion Energy Postdoctoral Research Program administered by ORISE.

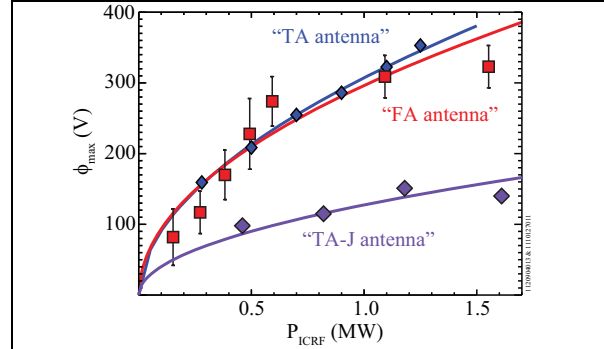


Figure 11: The measured maximum RF enhanced plasma potential for both the FA (red squares) and TA (blue diamonds) antenna are similar. The RF enhanced plasma potential from the toroidally aligned antenna at J port has lower RF enhanced plasma potential.

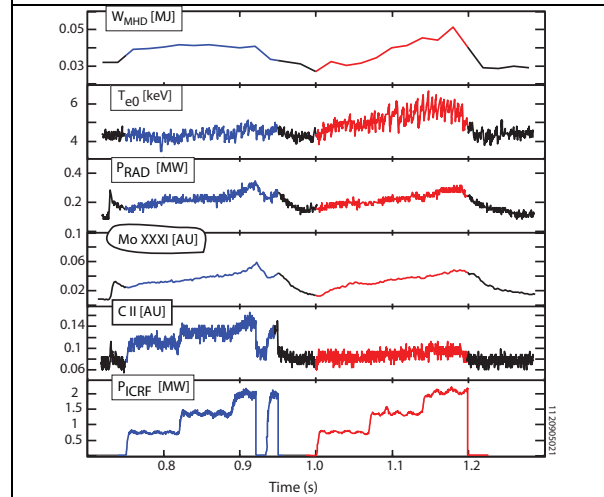


Figure 12: Time histories of the stored plasma energy, central electron temperature, core radiated power, core molybdenum XXXI, carbon II, and RF power trace. From 0.6-0.95 s, monopole phase (blue) is utilized while from 1-1.2 s dipole phasing is utilized. The stored energy and central electron temperature response is proportional to RF power. The radiate power and molybdenum response is similar while the carbon II signal responds promptly to monopole phase.

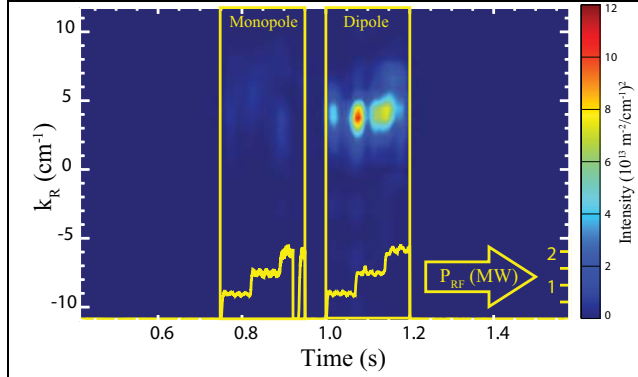


Figure 13: Spectrogram of phase contrast imaging signal shows that the mode converted wave is present in the plasma core only during the dipole (1-1.2 s) portion of the RF pulse.

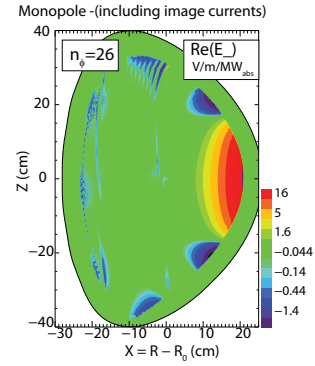


Figure 14: Full wave TORIC simulation for toroidal moden number of 26 shows the wave fails to penetrate to the plasma core.

REFERENCES

1. ITER Physics Expert Group on Energetic Particles, Heating, and Current Drive, Nucl. Fus. **39**, 2495 (1999).
2. J.R. Wilson et al., Phys. Rev. Lett. **75**, 842 (1995).
3. D.F.H. Start et al., Phys. Rev. Lett. **80**, 4681 (1998).
4. H. Bolt, V Barabash, G Federici, J Linke, A Loarte, J Roth, and K Sato, J. Nuclear Materials **307–311**, 43 (2002).
5. F.W. Perkins, Nuc. Fus. **29**, 583 (1989).
6. D. A. D'Ippolito, J. R. Myra, J. Jacquinot, and M. Bures, Phys. Fluids B **5**, 3603 (1993).
7. S.J. Wukitch, M. Garrett, H. Barnard, B. LaBombard, Y. Lin, B. Lipschultz, E. Marmor et al., Proc. 23rd IAEA Fusion Energy Conf., (Daejeon), EX-D/P3-37 (2010).
8. V. Bobkov et al., Proc. 24th IAEA Fusion Energy Conf., (San Diego), EX/P5-19 (2012).
9. M. Bures, J. Jacquinot, K. Lawson, M. Stamp, H. P. Summers, D. A. D'Ippolito, and J. R. Myra. Plasma Phys. Control. Fusion **33**, 937 (1991). doi:10.1088/0741-3335/33/8/005.
10. Czarnecka, A., F. Durodié, A. C. A. Figueiredo, K. D. Lawson, E. Lerche, M.-L. Mayoral, J. Ongena, et al., Plasma Phys. Control. Fusion **54**, 074013 (2012). doi:10.1088/0741-3335/54/7/074013.
11. X. Litaudon, J.M. Bernard, L. Colas, R. Dumont, A. Argouarch, H. Bottollier-Curtet, S. Brémond et al., "Physics and Technology in the Ion-cyclotron Range of Frequency on Tore Supra and TITAN test facility: implication for ITER," Nucl. Fusion (accepted).
12. P. Jacquet, F. Marcotte, L. Colas, G. Arnoux, V. Bobkov, Y. Corre, S. Devaux, et al., J. Nuclear Mater. **438**, S379 (2013). doi:10.1016/j.jnucmat.2013.01.075.
13. L. Colas et al., Proc. 20th PSI Conf. Aachen 2012 P1-5, submitted to J. Nuclear Material.
14. B. Lipschultz, D. A. Pappas, B. LaBombard, J. E. Rice, D. Smith, and S.J. Wukitch, Nucl. Fusion **41**, 585 (2001).
15. D. A. D'Ippolito, J. R. Myra, J. H. Rogers, K. W. Hill, J. C. Hosea, R. Majeski, G. Schilling, et al., Nuclear Fusion **38**, 1543 (1998). doi:10.1088/0029-5515/38/10/311.
16. Garrett, M.L., and S.J. Wukitch, Fus. Eng. Design **87**, 1570 (2012). doi:10.1016/j.fusengdes.2012.04.011.
17. P. H. Probert and R. P. Majeski, Rev. Sci. Instr. **68**, 1168 (1997) doi:10.1063/1.1147879.
18. S. J. Wukitch, M. L. Garrett, R. Ochoukov, J. L. Terry, A. Hubbard, B. Labombard, C. Lau, et al. Phys. Plasmas **20**, 056117 (2013). doi:10.1063/1.4803882.
19. E. Nelson-Melby, M. Porkolab, P. T. Bonoli, Y. Lin, A. Mazurenko, and S. J. Wukitch. Phys. Rev. Lett. **90**, 155004 (2003) doi:10.1103/PhysRevLett.90.155004.
20. N. Tsujii, M. Porkolab, P. T. Bonoli, Y. Lin, J. C. Wright, S. J. Wukitch, E. F. Jaeger, D. L. Green, and R. W. Harvey, Phys. Plasmas **19**, 082508 (2012) doi:10.1063/1.4745613.
21. M.D Carter, D.A Rasmussen, P.M Ryan, G.R Hanson, D.C Stallings, D.B Batchelor, T.S Bigelow, et al., Nuc. Fusion **36**, 209 (1996). doi:10.1088/0029-5515/36/2/I08.
22. M. Brambilla, Plasma Phys. Control. Fus. **41**, 1 (1999). doi:10.1088/0741-3335/41/1/002.